Supporting Information

Volatile and Nonvolatile Resistive Switching in Lateral 2D Molybdenum Disulfide-Based Memristive Devices

Sofia Cruces[#], Mohit D. Ganeriwala[†], Jimin Lee[#], Ke Ran[¥,§,Ω] , Janghyun Jo[Ω], Lukas Völkel[#], Dennis Braun[#], Bárbara Canto[¥], Enrique G. Marín[†], Holger Kalisch[‡], Michael Heuken[‡,¶], Andrei Vescan[‡], Rafal E. Dunin-Borkowski[Ω], Joachim Mayer[§,Ω], Andrés Godoy[†], Alwin Daus[//], and Max C. Lemme[#,¥]*

[#] Chair of Electronic Devices, RWTH Aachen University, Otto-Blumenthal-Str. 25, 52074 Aachen, Germany.

[†] Department of Electronics and Computer Technology, Facultad de Ciencias, Universidad de Granada, 18071, Granada, Spain.

[¥] AMO GmbH, Advanced Microelectronic Center Aachen, Otto-Blumenthal-Str. 25, 52074 Aachen, Germany.

§ Central Facility for Electron Microscopy, RWTH Aachen University, Ahornstr. 55, 52074, Aachen, Germany.

Ω Ernst Ruska-Centre for Microscopy and Spectroscopy with Electrons (ER-C), Forschungszentrum Jülich GmbH, Wilhelm-Johnen-Str., 52425 Jülich, Germany.

‡ Compound Semiconductor Technology, RWTH Aachen University, Sommerfeldstr. 18, 52074 Aachen, Germany.

¶ AIXTRON SE, Dornkaulstr. 2, 52134 Herzogenrath, Germany.

‖ Institute of Semiconductor Engineering, University of Stuttgart, Pfaffenwaldring 47, 70569 Stuttgart, Germany.

* Corresponding author. Email: max.lemme@eld.rwth-aachen.de (MCL)

This file includes:

Materials and Methods

Metal–organic chemical vapor deposition (MOCVD) of MoS_2

Highly uniform multi-layered molybdenum disulfide (MoS_2) has been epitaxially grown in a commercial AIXTRON planetary hot-wall reactor in 10 × 2" configuration on c-plane sapphire substrates (with a 0.2° offcut toward m-plane). First, a substrate desorption at 970 °C in a pure H_2 atmosphere has been performed. Afterward, growth has been carried out at a substrate temperature of 750 °C for 24 h, with nitrogen as the carrier gas and at a pressure of 30 hPa. The precursor flows have been set to 19 nmol/min for molybdenum hexacarbonyl (MCO) and 19 µmol/min for di-tert-butyl sulfide (DTBS).

Device Fabrication

MoS_2 grown on 2" sapphire by MOCVD was transferred onto 2 × 2 cm^2 Si chips covered with 275 nm thermal SiO_2 thermally grown on Si wafers with p-doping of 1–10 Ω·cm. Poly(methyl methacrylate) (PMMA) was spin-coated on top of the MoS_2 before being released from the sapphire substrate in deionized water.[1] For both electrodes the AZ5214E JP photoresist from Merck Performance Materials GmbH was used. The palladium (Pd) electrodes were defined using optical contact lithography with an EVG 420 Mask Aligner and the silver (Ag) ones with a Microtech LW405C laser writer. The asymmetric Pd (50 nm) and Ag (50 nm)/aluminum (Al) (50 nm) electrodes were deposited via electron-beam evaporation (e-beam) in a tool from FHR Anlagenbau GmbH and subsequently lifted in acetone at room temperature. Finally, the channels were patterned via CF_4 (20 sccm)/O_2 (10 sccm) reactive ion etching (RIE) in an Oxford Instruments Plasma Lab System 100 tool. The resist was stripped in acetone at 60 °C for 1 h. For the in-situ experiments, an extra 80 nm aluminum oxide (Al_2O_3) layer was deposited via e-beam in a tool from FHR Anlagenbau GmbH. The Al_2O_3 layer is required not only to protect the MoS_2

from the ion beam during the focused ion beam (FIB) preparation but also to avoid direct contact of the platinum (Pt) protection layer with both electrodes and MoS_2 layers. If the Pt protection layer is directly in contact with both electrodes, current would bypass the MoS_2 layers, and a short circuit would be observed. For the same reason, the Pt protection layer was removed in the center of the lamella (on top of the MoS_2 and the Al_2O_3 layer as shown in Figure S8c).

Material and Device Characterization

Optical microscope images were recorded with a Leica INM100 microscope and a Keyence 3D Laser Scanning microscope VK- X3000. Raman and photoluminescence (PL) measurements were performed with a WiTec alpha300R Raman spectrometer with an excitation laser wavelength of 532 nm and 1 mW laser power. TEM specimens were prepared by FIB milling using an FEI Strata400 system with gallium (Ga) ion beam. Transmission electron microscopy (TEM) analysis was conducted with a JEOL JEM F200 instrument at 200 kV. *In-situ* TEM was conducted with a FEI Titan G2 80-200 ChemiSTEM microscope at 200 kV equipped with an XFEG, a probe Cs corrector and a super-X energy-dispersive X-ray spectroscopy (EDXS) system. A voltage bias was applied *in-situ* to the TEM lamella in the TEM using a Nanofactory STM-TEM specimen holder connected to an external "Keithley 2602A" source meter. Atomic force microscopy (AFM) measurements were conducted with a Dimension Icon AFM from Bruker Instruments using a tip with 26 N/m as force constant and the frequency variation between 200 and 400 kHz (OTESPA) in tapping mode in air and at room temperature.

Electrical Measurements

Electrical measurements were performed in a LakeShore probe station connected to a semiconductor parameter analyzer (SPA) "Keithley 4200A-SCS" with two source measure unit (SMU) cards "Keithley 4200-SMU", each connected to a preamplifier "Keithley 4200-PA" from

Tektronix. A voltage bias was applied to the Ag/Al active electrode, and the Pd electrode was grounded. Current-voltage *(I–V)* measurements were conducted by sweeping the voltage from 0 V to a positive maximum voltage V_{max} and back to 0 V. For the nonvolatile measurements the same was applied in the negative polarity for resetting the devices. The current is limited by an external current limiter within the semiconductor parameter analyzer. Pulse experiments were performed by supplying a voltage to the Ag/Al active electrode (channel 1) and measuring the output current over time in channel 2 (Pd electrode). Temperature-dependent measurements were conducted for each temperature in two steps. First, 10 measurement points at a constant read voltage of 100 mV were collected to extract the device resistance. Second, a forward sweep from −0.2 V to 0.2 V was applied.

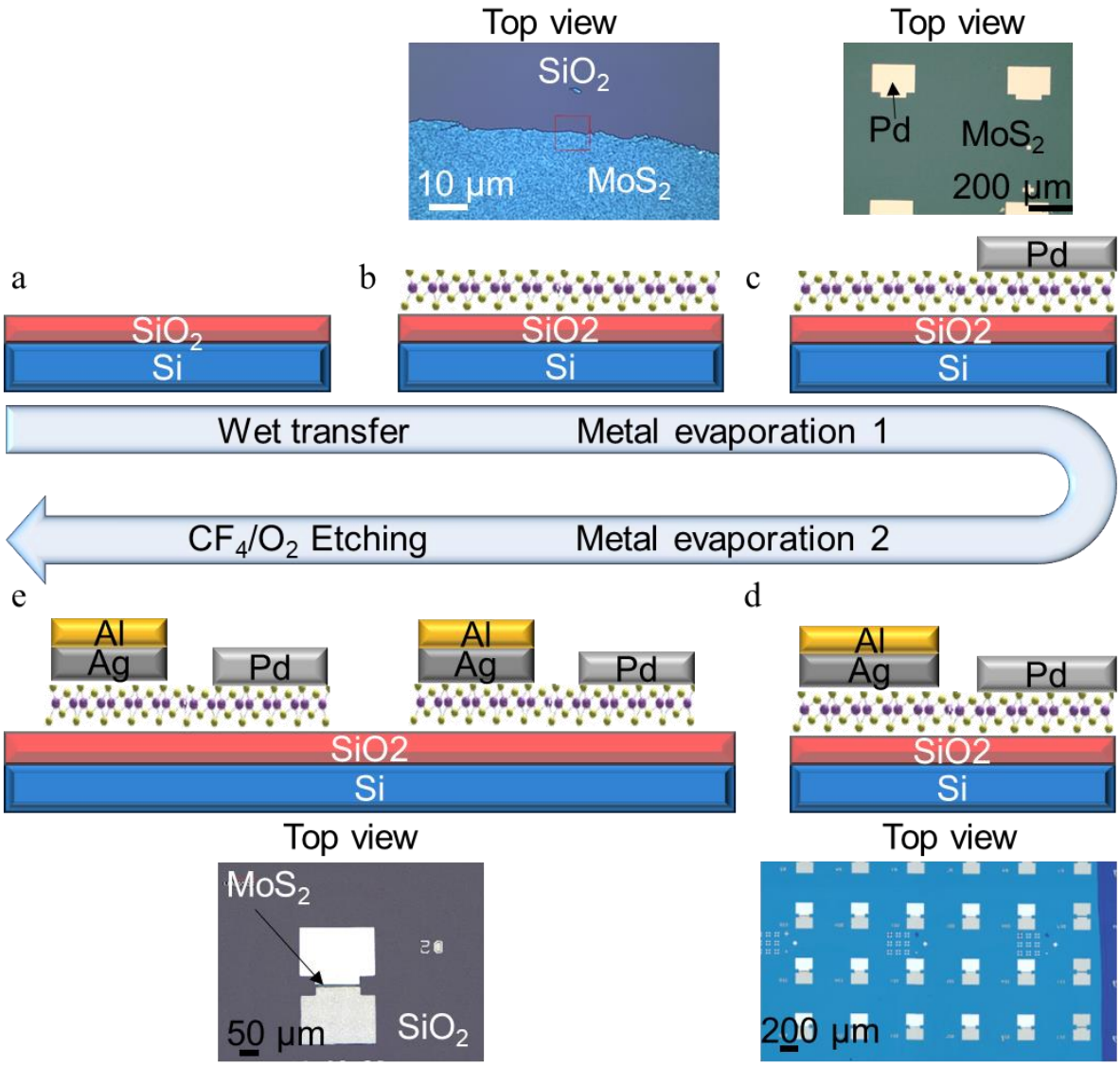

Supplementary Figure S1. Fabrication process flowchart. (a) Clean SiO_2/Si substrate. (b) Wet transfer of MoS_2 film from sapphire substrate to SiO_2/Si. Top view optical microscopy (OM) image of MoS_2 on SiO_2 after transfer. (c) Electron beam (e-beam) evaporation of the Pd metal contact after photolithography with negative photoresist and lift-off. The OM image shows a top view of the Pd electrode on MoS_2. (d) E-beam evaporation of Ag and Al on top as capping layer after photolithography with negative photoresist and lift-off. The OM shows a top view of multiple devices with both electrodes on top of the MoS_2 film. (e) Reactive ion etching of the MoS_2 active

areas with CF_4/O_2 after photolithography with positive photoresist followed by resist stripping in acetone. The OM images show a device after photoresist stripping and a close up to the gap between electrodes.

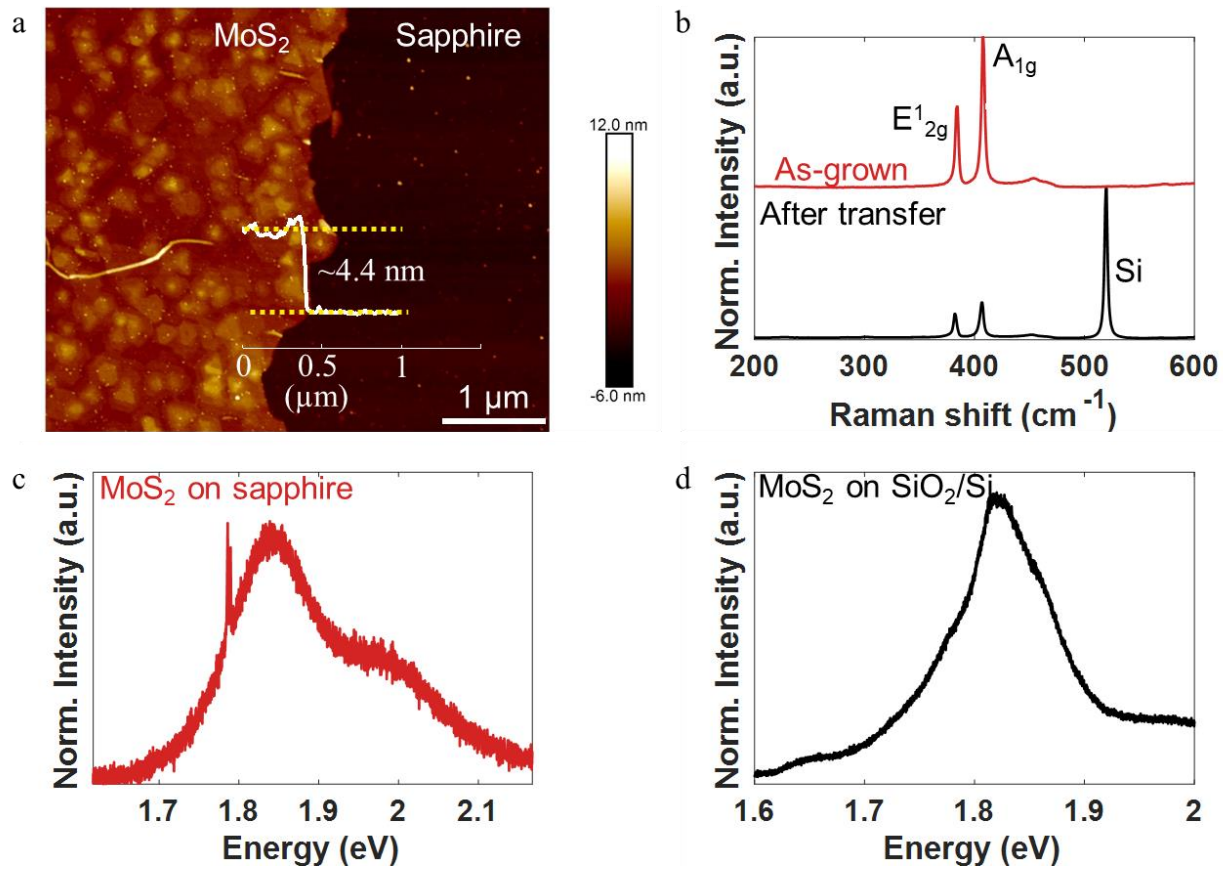

Supplementary Figure S2. MoS_2 material characterization. (a) Atomic force microscopy (AFM) image of the as-grown MoS_2 on sapphire. The inset height profile shows a thickness of ~4.4 nm. (b) Raman spectra of as-grown MoS_2 on sapphire and after transfer on a SiO_2/Si substrate. The extracted peaks for the as-grown MoS_2 on sapphire were 383.9 cm^{-1} and 407.9 cm^{-1} for the E^1_{2g} and A_{1g} peaks, respectively. In the case of the transferred MoS_2 onto an SiO_2/Si substrate, the obtained values were 382.4 cm^{-1} and 406.5 cm^{-1} for the E^1_{2g} and A_{1g} peaks, respectively. All the extracted values match those previously reported for four layers or bulk.[2,3] PL spectrum of (c) as-grown MoS_2 on sapphire showing both PL peaks and (d) after transfer on a SiO_2/Si substrate. The PL peak position located at 1.82 eV is in good agreement with the theoretical value for multilayer MoS_2 [4–6], indicating high crystal quality of the transferred material.

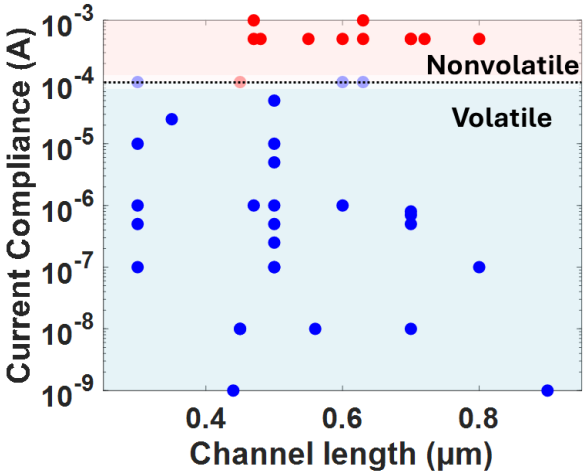

Supplementary Figure S3. Distribution diagram of the current compliance (CC) values. For cc values of 100 μA and under the devices showed volatile behavior, whereas for over 100 μA the devices displayed non-volatile characteristics.

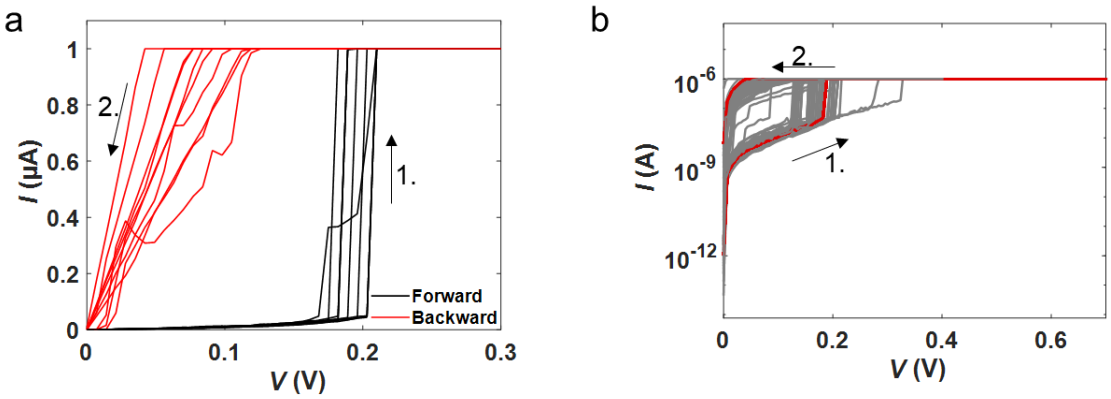

Supplementary Figure S4. Volatile *I-V* curves on a linear and logarithmic scale. (a) 10 consecutive volatile resistive switching (RS) curves at 1 μA CC in linear scale. The forward sweep is marked in black, and the backward sweep is marked in red. (b) 60 consecutive volatile RS cycles at 1 μA CC in logarithmic scale. The first sweep is marked in red.

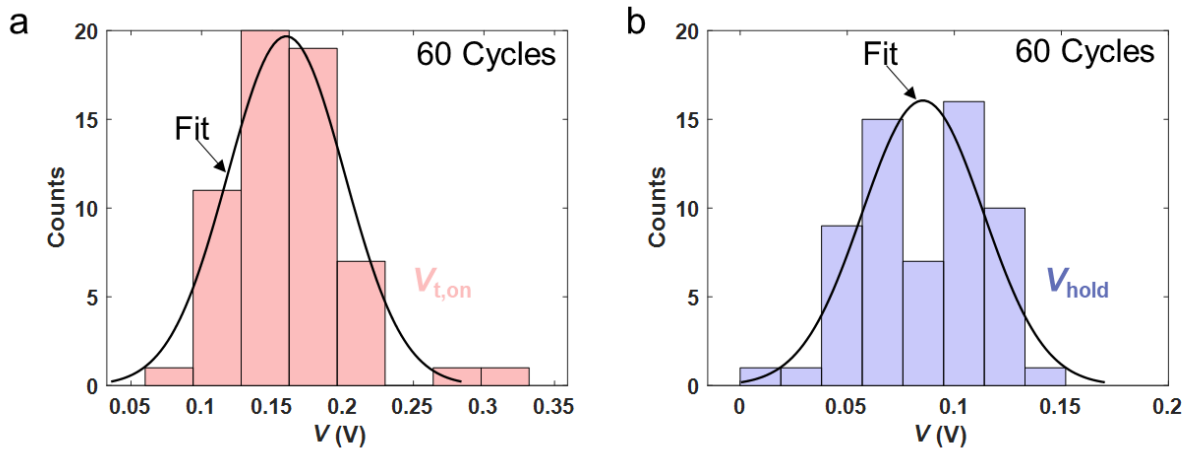

Supplementary Figure S5. Statistical analysis of switching voltages for $V_{t,on}$ and V_{hold}. (a) Histogram and Gaussian fit for $V_{t,on}$ derived from 60 volatile RS data points. (b) Histogram and Gaussian fit for V_{hold} derived from 60 volatile RS data points. The statistical distributions of the $V_{t,on}$ and V_{hold} show low mean voltage values and low standard deviations (σ) of 0.16 ± 0.04 V and 0.085 ± 0.03 V, respectively.

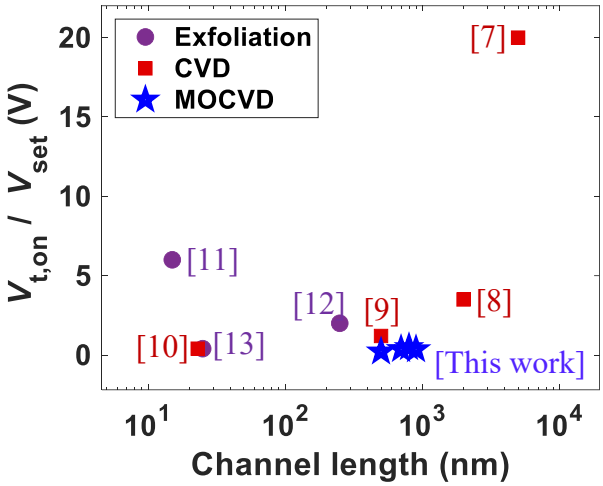

Supplementary Figure S6. Comparison of our work with other similar 2D-based literature. Benchmarking plot showing the key values of our devices with other similar ones reported in the literature. [7–13]

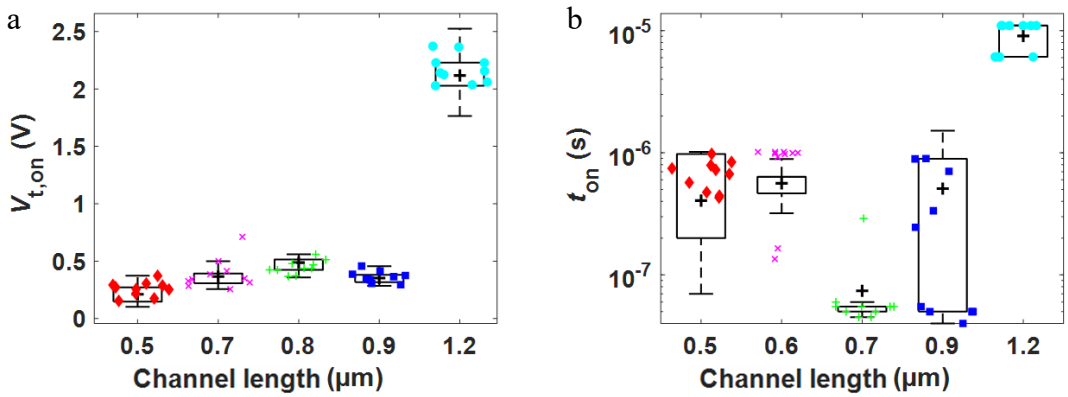

Supplementary Figure S7. Influence of the channel length (gap size). (a) $V_{t,on}$ dependence upon channel length variation. (b) Switching time versus channel length. The $V_{t,on}$ decreases with decreasing channel lengths which is in good agreement with the literature. [12–14]

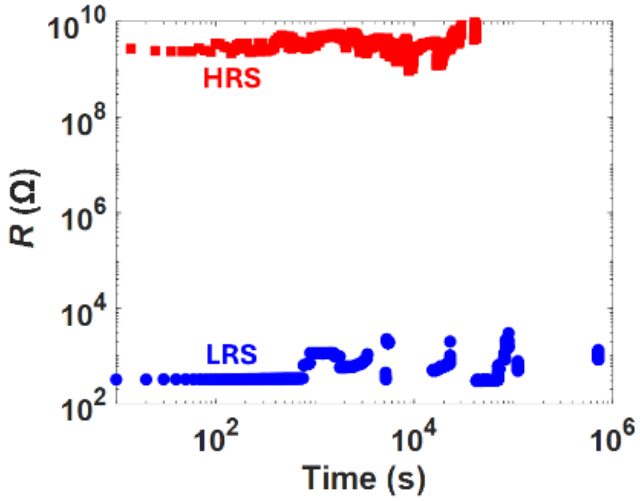

Supplementary Figure S8. Retention time of the HRS and the LRS of a device. The device remained in the LRS for ~8 days until we manually reset it for measuring the HRS for ~12 h. The measurement was manually stopped to be able to use the device for other electrical measurements and it was still functional.

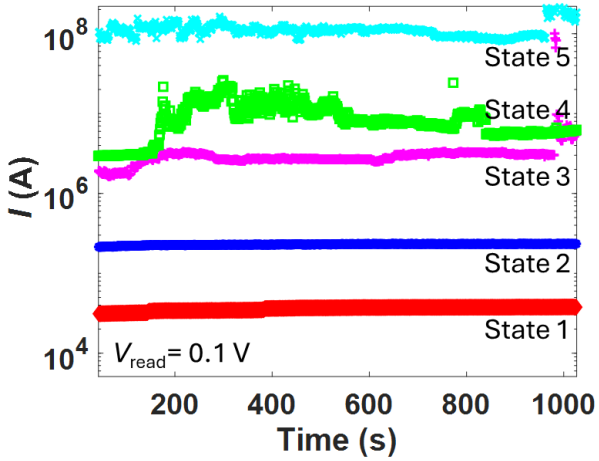

Supplementary Figure S9. Retention characteristics of 5 different LRS states of a device. Current measurement over time for 5 different LRS states, evidencing the goodness of the retention characteristics of our nonvolatile RS for at least 1000 s.

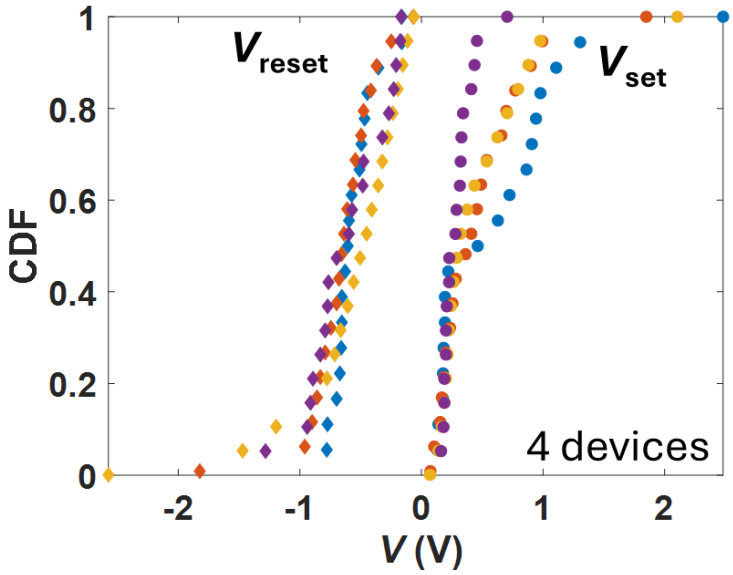

Supplementary Figure S10. Device-to-device variability. CDFs of the V_{set} and the V_{reset} for four different devices. The V_{reset} shows less variation from device-to-device than V_{set}. The calculated standard error is 5.07% and 4.4% for V_{set} and V_{reset}, respectively.

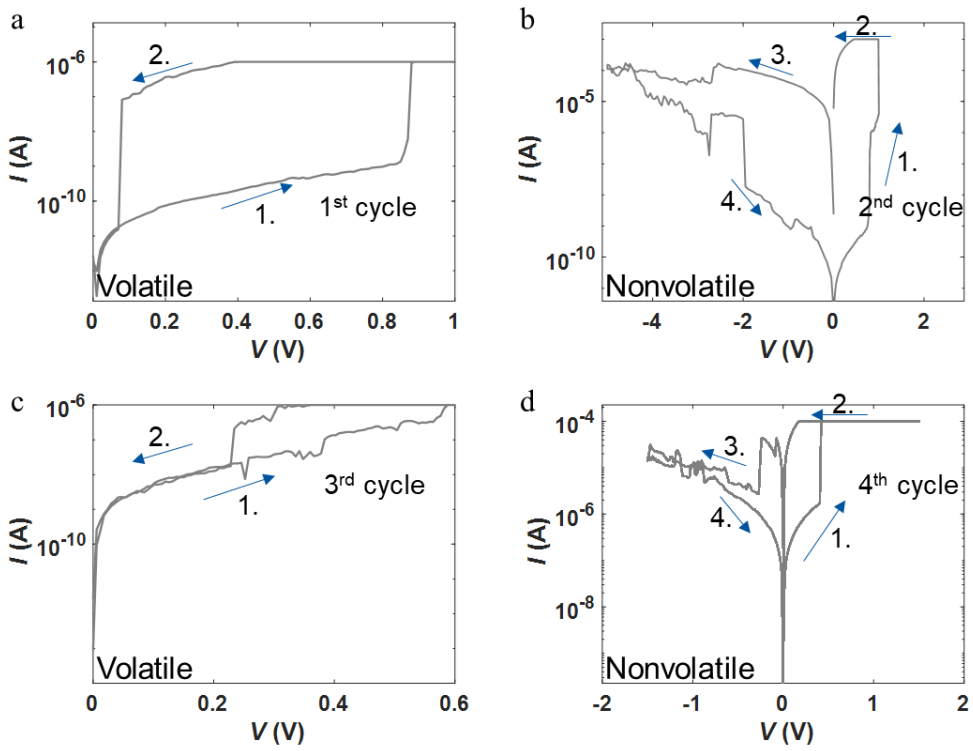

Supplementary Figure S11. Transition from volatile to nonvolatile back and forth. (a) One volatile threshold RS *I-V* sweep with a CC at 1 μA (1st cycle). (b) One nonvolatile RS *I-V* sweep with a CC at 1 mA after the first one in (a) showing both set and reset processes (2nd cycle). (c) One volatile threshold RS *I-V* sweep with a CC at 1 μA conducted after the nonvolatile RS cycle in (b) (3rd cycle). (d) One nonvolatile RS *I-V* sweep (4th cycle) with a CC at 1 mA. The arrows show the voltage sweep direction.

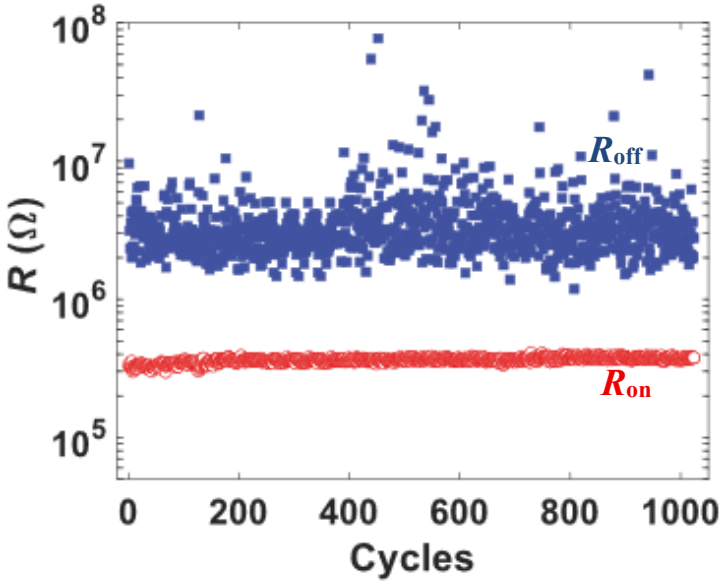

Supplementary Figure S12. Endurance showing the R_{on} and R_{off} of volatile RS under PVS. The cycling endurance was assessed by measuring the ON-state (R_{on}) and the OFF-state resistance (R_{off}) for every switching cycle. The R_{on} values exhibit a low cycle-to-cycle variability with a R_{off}/R_{on} ratio of over 12. Some variations in the R_{off} values are introduced by the measurement setup, which operates near its noise limit.

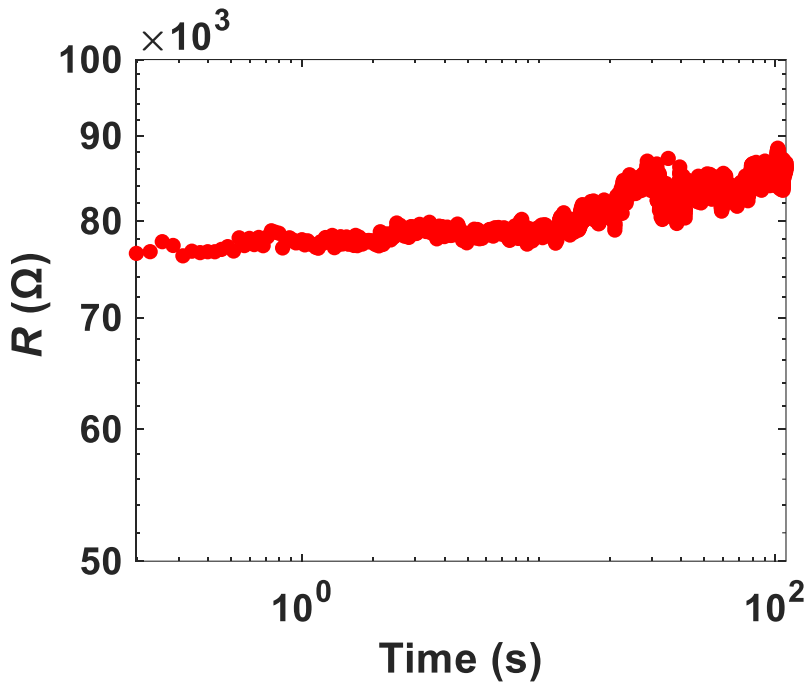

Supplementary Figure S13: Low-resistance state (LRS) retention over 100 s after continuous pulsed stimulation. Retention of the LRS with a DC measurement for 4096 data points.

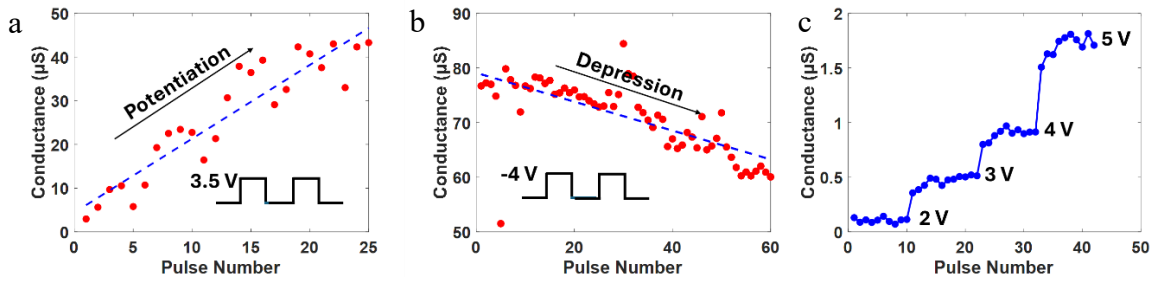

Supplementary Figure S14: Synaptic characteristics of a device. (a) Postsynaptic conductance (PSC) as a function of the number of positive bias pulses, showcasing long-term potentiation (LTP). (b) PSC as a function of the number of negative bias pulses evidencing long-term depression (LTD). (c) PSC as a function of the number of pulses with varying pulse amplitude from 2 V and up to 5 V.

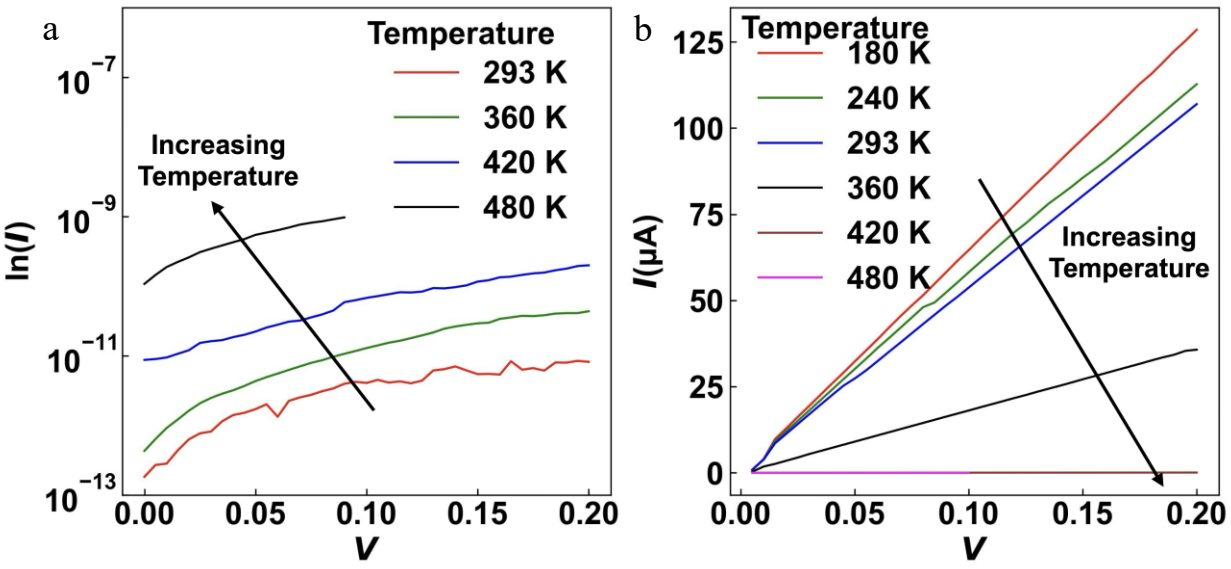

Supplementary Figure S15. Temperature dependent measurements for the HRS and the LRS. (a) In the HRS the current increases with increasing temperature, which is characteristic of transport through the MoS_2 channel and SCLC.[15] (b) In the LRS the current decreases with increasing temperature, indicating a negative temperature coefficient of resistivity which is characteristic of transport through a metallic CF.[16] Furthermore, the temperature coefficient of resistance (TCR) was calculated. Note that, the R(T) dependence is derived for an ideal, uniform conductor that does not undergo physical changes during temperature variations. In the RS case, resistance itself evolves due to morphological changes in the filament, which are likely to contribute to the change in resistance with increasing temperature. Nevertheless, at low temperatures and under low-voltage conditions atomic movement is expected to be minimal. Therefore, assuming no morphology change, the TCR using the measured resistances: R=1.55 kΩ at T=180 K, R=1.72 kΩ at T=240 K and R=1.85 kΩ at T=293 K was calculated. From these values, the estimated temperature coefficient under a linear regression is $\alpha \approx -0.0018\ K^{-1}$, which is close to the known value for Ag ($\alpha \approx -0.002\ K^{-1}$). Therefore, based on the experimental evidence

and comparative analysis, these results reasonably support the conclusion that a metallic filament is formed during the switching process.

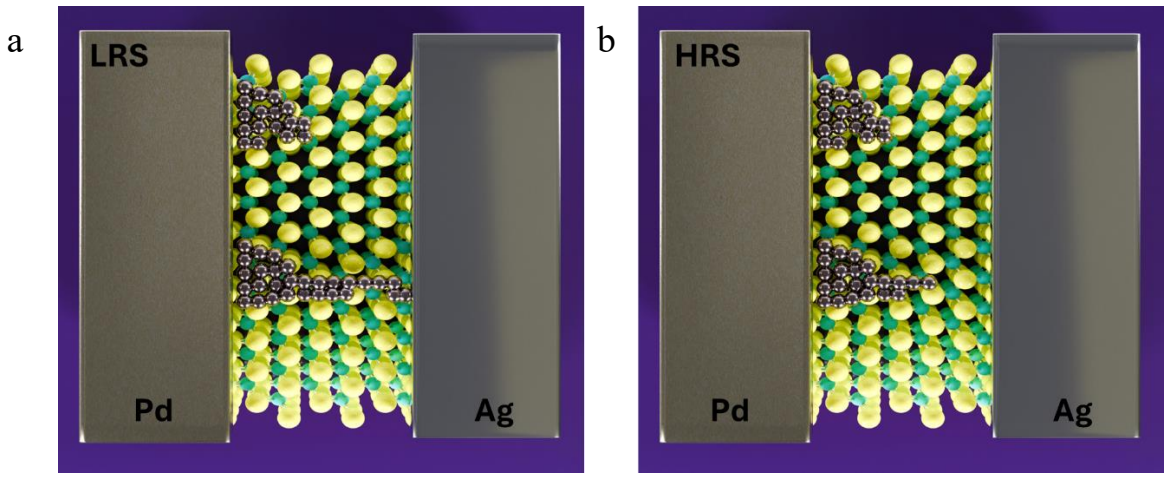

Supplementary Figure S16. Top-view schematic of the RS mechanism of our MoS_2-based memristor. (a) Top view of a device in the LRS. (b) Top view of a device in the HRS.

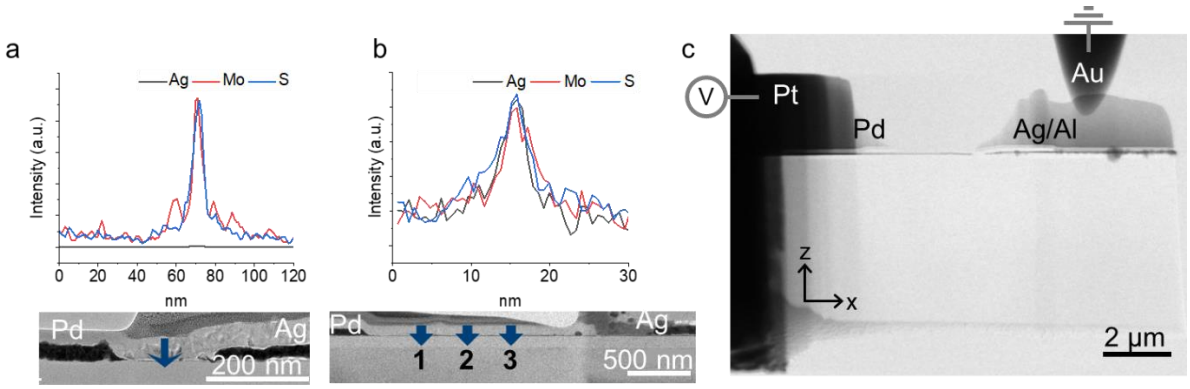

Supplementary Figure S17. EDXS line profiles, HRTEM and lamella for *in-situ* TEM electrical measurements. The EDXS line profiles showing the intensities of corresponding characteristic X-rays were recorded along the vertical direction pointed by the blue arrows marked in the cross-section TEM images. (a) EDXS line profile of a lamella in the HRS as shown in the TEM image, before any electrical measurement is carried out. The profile for Ag is flat, proving the absence of Ag within the MoS_2 and in the channel between electrodes. (b) EDXS line profile of a lamella in the LRS taken at position 1 as depicted in the TEM image. The intensity profile of Ag coincides with those from Mo and S, proving the presence of Ag within the MoS_2 channel. (c) TEM image of one lamella used for the *in-situ* TEM measurements. The Pd electrode was biased while the Ag active electrode was grounded.

Supplementary References

(1) Rademacher, N.; Reato, E.; Völkel, L.; Grundmann, A.; Heuken, M.; Kalisch, H.; Vescan, A.; Daus, A.; Lemme, M. C. CVD Graphene-MoS2 Van Der Waals Heterostructures on the Millimeter-Scale. *Micro and Nano Engineering* **2024**, *23*, 100256. https://doi.org/10.1016/j.mne.2024.100256.

(2) Lee, C.; Yan, H.; Brus, L. E.; Heinz, T. F.; Hone, J.; Ryu, S. Anomalous Lattice Vibrations of Single- and Few-Layer MoS_2. *ACS Nano* **2010**, *4* (5), 2695–2700. https://doi.org/10.1021/nn1003937.

(3) Li, H.; Zhang, Q.; Yap, C. C. R.; Tay, B. K.; Edwin, T. H. T.; Olivier, A.; Baillargeat, D. From Bulk to Monolayer MoS_2 : Evolution of Raman Scattering. *Adv Funct Materials* **2012**, *22* (7), 1385–1390. https://doi.org/10.1002/adfm.201102111.

(4) Sarkar, S.; Mathew, S.; Chintalapati, S.; Rath, A.; Panahandeh-Fard, M.; Saha, S.; Goswami, S.; Tan, S. J. R.; Loh, K. P.; Scott, M.; Venkatesan, T. Direct Bandgap-like Strong Photoluminescence from Twisted Multilayer MoS_2 Grown on $SrTiO_3$. *ACS Nano* **2020**, *14* (12), 16761–16769. https://doi.org/10.1021/acsnano.0c04801.

(5) Eda, G.; Yamaguchi, H.; Voiry, D.; Fujita, T.; Chen, M.; Chhowalla, M. Photoluminescence from Chemically Exfoliated MoS_2. *Nano Lett.* **2011**, *11* (12), 5111–5116. https://doi.org/10.1021/nl201874w.

(6) Scheuschner, N.; Ochedowski, O.; Kaulitz, A.-M.; Gillen, R.; Schleberger, M.; Maultzsch, J. Photoluminescence of Freestanding Single- and Few-Layer MoS 2. *Phys. Rev. B* **2014**, *89* (12), 125406. https://doi.org/10.1103/PhysRevB.89.125406.

(7) Sangwan, V. K.; Lee, H.-S.; Bergeron, H.; Balla, I.; Beck, M. E.; Chen, K.-S.; Hersam, M. C. Multi-Terminal Memtransistors from Polycrystalline Monolayer Molybdenum Disulfide. *Nature* **2018**, *554* (7693), 500–504. https://doi.org/10.1038/nature25747.

(8) Sangwan, V. K.; Jariwala, D.; Kim, I. S.; Chen, K.-S.; Marks, T. J.; Lauhon, L. J.; Hersam, M. C. Gate-Tunable Memristive Phenomena Mediated by Grain Boundaries in Single-Layer MoS2. *Nature Nanotech* **2015**, *10* (5), 403–406. https://doi.org/10.1038/nnano.2015.56.

(9) Hao, S.; Ji, X.; Zhong, S.; Pang, K. Y.; Guan Lim, K.; Chong Chong, T.; Zhao, R. A Monolayer Leaky Integrate- and Fire Neuron for 2D Memristive Neuromorphic Networks. *Adv. Electron. Mater.* **2020**, *6* (4), 1901335.

(10) Dev, D.; Krishnaprasad, A.; Shawkat, M. S.; He, Z.; Das, S.; Fan, D.; Chung, H.-S.; Jung, Y.; Roy, T. 2D MoS_2 -Based Threshold Switching Memristor for Artificial Neuron. *IEEE Electron Device Lett.* **2020**, *41* (6), 936–939. https://doi.org/10.1109/LED.2020.2988247.

(11) Li, C.; Xu, T.; Pan, R.; Bao, S.; Yin, K.; Shen, J.; Zhu, Y.; Hou, S.; Sun, L. Electric Field-Dependent Evolution Dynamics of Conductive Filaments in 2D Material-Based Planar Memristors. *ACS Nano* **2024**, *18* (46), 32196–32204. https://doi.org/10.1021/acsnano.4c11598.

(12) Yin, S.; Luo, Z.; Li, Q.; Xiong, C.; Liu, Y.; Singh, R.; Zeng, F.; Zhong, Y.; Zhang, X. Emulation of Learning and Memory Behaviors by Memristor Based on Ag Migration on 2D MoS_2 Surface. *Phys. Status Solidi A* **2019**, *216* (14), 1900104. https://doi.org/10.1002/pssa.201900104.

(13) Farronato, M.; Melegari, M.; Ricci, S.; Hashemkhani, S.; Bricalli, A.; Ielmini, D. Memtransistor Devices Based on MoS_2 Multilayers with Volatile Switching Due to Ag Cation Migration. *Adv Elect Materials* **2022**, *8* (8), 2101161. https://doi.org/10.1002/aelm.202101161.

(14) Cruces, S.; Ganeriwala, M. D.; Lee, J.; Völkel, L.; Braun, D.; Grundmann, A.; Ran, K.; González Marín, E.; Kalisch, H.; Heuken, M.; Vescan, A.; Mayer, J.; Godoy, A.; Daus, A.; Lemme, M. C. Volatile MoS_2 Memristors with Lateral Silver Ion Migration for Artificial Neuron Applications. *Small Science* **2025**, 2400523. https://doi.org/10.1002/smsc.202400523.
(15) Daus, A.; Jaikissoon, M.; Khan, A. I.; Kumar, A.; Grady, R. W.; Saraswat, K. C.; Pop, E. Fast-Response Flexible Temperature Sensors with Atomically Thin Molybdenum Disulfide. *Nano Lett.* **2022**, *22* (15), 6135–6140. https://doi.org/10.1021/acs.nanolett.2c01344.
(16) Ashcroft, N. W.; Mermin, N. D. *Solid State Physics*; Saunders college publ: Fort Worth Philadelphia San Diego [etc.], 1976.